nature materials

PROGRESS ARTICLE

PUBLISHED ONLINE: 20 FEBRUARY 2014 | DOI: 10.1038/NMAT3816

Charge-extraction strategies for colloidal quantum dot photovoltaics

Xinzheng Lan[1,2], Silvia Masala[1,3] and Edward H. Sargent[1]*

The solar-power conversion efficiencies of colloidal quantum dot solar cells have advanced from sub-1% reported in 2005 to a record value of 8.5% in 2013. Much focus has deservedly been placed on densifying, passivating and crosslinking the colloidal quantum dot solid. Here we review progress in improving charge extraction, achieved by engineering the composition and structure of the electrode materials that contact the colloidal quantum dot film. New classes of structured electrodes have been developed and integrated to form bulk heterojunction devices that enhance photocharge extraction. Control over band offsets, doping and interfacial trap state densities have been essential for achieving improved electrical communication with colloidal quantum dot solids. Quantum junction devices that not only tune the optical absorption spectrum, but also provide inherently matched bands across the interface between p- and n-materials, have proven that charge separation can occur efficiently across an all-quantum-tuned rectifying junction.

Photovoltaic devices — which convert abundant, free solar radiation into electric power — are increasingly required to offer the simultaneous combination of low cost and high efficiency. Si-based solar cells[1], vapour-phase-processed thin-film solar cells such as CdS/CdTe (ref. 2) and next-generation solution-processed solar cells based on molecular sensitizers[3], organic materials[4], hybrid organic–inorganic systems[5] and quantum dots[6,7] all seek to fulfil this goal.

Efficient harvesting of the wide dispersion of photon energies that make up the broad solar spectrum represents a crucial frontier for low-cost, high-efficiency solar cells (Fig. 1a). Colloidal quantum dots (CQDs) — solution-synthesized and -processed semiconductor nanocrystals that provide a nanoparticle-size-dependent bandgap — offer an avenue to tandem and multi-junction solar cells that make excellent use of the dispersion of solar fluence as a function of photon energy[8,9] (Fig. 1a). They also show promise in multiple exciton generation[10] as well as photon up- and downconversion[11], technologies that, like the multi-junction strategy, offer a roadmap beyond the Shockley–Queisser limit[12].

Since early reports of promising size-effect-tuned devices in 2005[7], CQD solar cells have seen rapid progress, much of it owing to improvements in the electronic material properties of the quantum dot solid. The deepened understanding and exploitation of the interaction between inorganic quantum dots and organic, inorganic, or hybrid ligand and crosslinker systems has played a central role in performance advances[13–18]. The ligand exchange process has been tuned to optimize inter-quantum-dot spacing, enhancing charge-carrier mobility[7,19,20]. In parallel, any states that lie within the bandgap of the quantum solid — including trap states attributable to the large surface area in the nanostructured solid — are now clearly recognized to play a role in limiting present-day performance[21]. This has motivated the development of new strategies to achieve improved surface passivation, including atomic and hybrid organic–inorganic ligand passivation[8,13,20,22–25].

Parallel to perfecting the light-absorbing quantum dot solid, there lies another highly promising axis for improving device performance. This relates to engineering the driving force that achieves high-quantum-efficiency extraction of electrons and holes to their respective electric contacts[26–28]. Progress in the materials chemistry and engineering of the charge-extracting constituents of the solar cell has recently produced significant improvements in CQD photovoltaics. In this Progress Article recent innovations in charge-extraction strategies for CQD photovoltaics are reviewed.

CQD device architectures and mechanisms

In early research in CQD solar cells, a Schottky structure was employed, wherein a layer of p-type CQDs was sandwiched between a transparent conductive oxide and a shallow-work-function metal[29–31]. A Schottky barrier was formed at the CQD/metal interface as a result of the large difference in material work functions. The resultant internal electric field arising from the Schottky barrier drove separation of photogenerated charge carriers.

Although Schottky devices are advantageous for their ease of fabrication and led the early advances in CQD photovoltaics, they suffer a number of limitations. The optical generation rate is highest on the ohmic-contacted side, resulting in a high density of photocarriers being produced far from the charge-separating Schottky interface, compromising efficient charge separation. Further, Fermi level pinning at the CQD/metal interface curtails the open-circuit voltage V_{OC}, and, at the same time, a small barrier for hole injection at the electron-extracting electrode produces undesired backwards recombination[8].

A depleted-heterojunction architecture was developed in 2010 to address these limitations. Typically, n-type wide-bandgap semiconductors such as TiO_2 (ref. 32), ZnO (ref. 33) and CdS (ref. 34) form a rectifying junction with a p-type CQD film (Fig. 1b). Electron–hole pair separation is promoted by the built-in electric field due to the junction as well as the type-II heterointerface that produces a cliff in the conduction band.

Despite rapid progress in the depleted heterojunction structure, the photovoltaic performance of CQD solar cells nevertheless remains limited by a compromise between light absorption and charge extraction. As seen in Fig. 1b, only photocarriers generated within one diffusion length of the edge of the depletion region are

[1]Department of Electrical and Computer Engineering, University of Toronto, 10 King's College Road, Toronto, Ontario M5S 3G4, Canada, [2]School of Materials Science and Engineering, Hefei University of Technology, 193 Tunxi Road, Hefei, Anhui Province, 230009, China, [3]Solar and Photovoltaic Engineering Research Center, King Abdullah University of Science and Technology, 4700 Thuwal 23955-6900, Saudi Arabia. *e-mail: ted.sargent@utoronto.ca

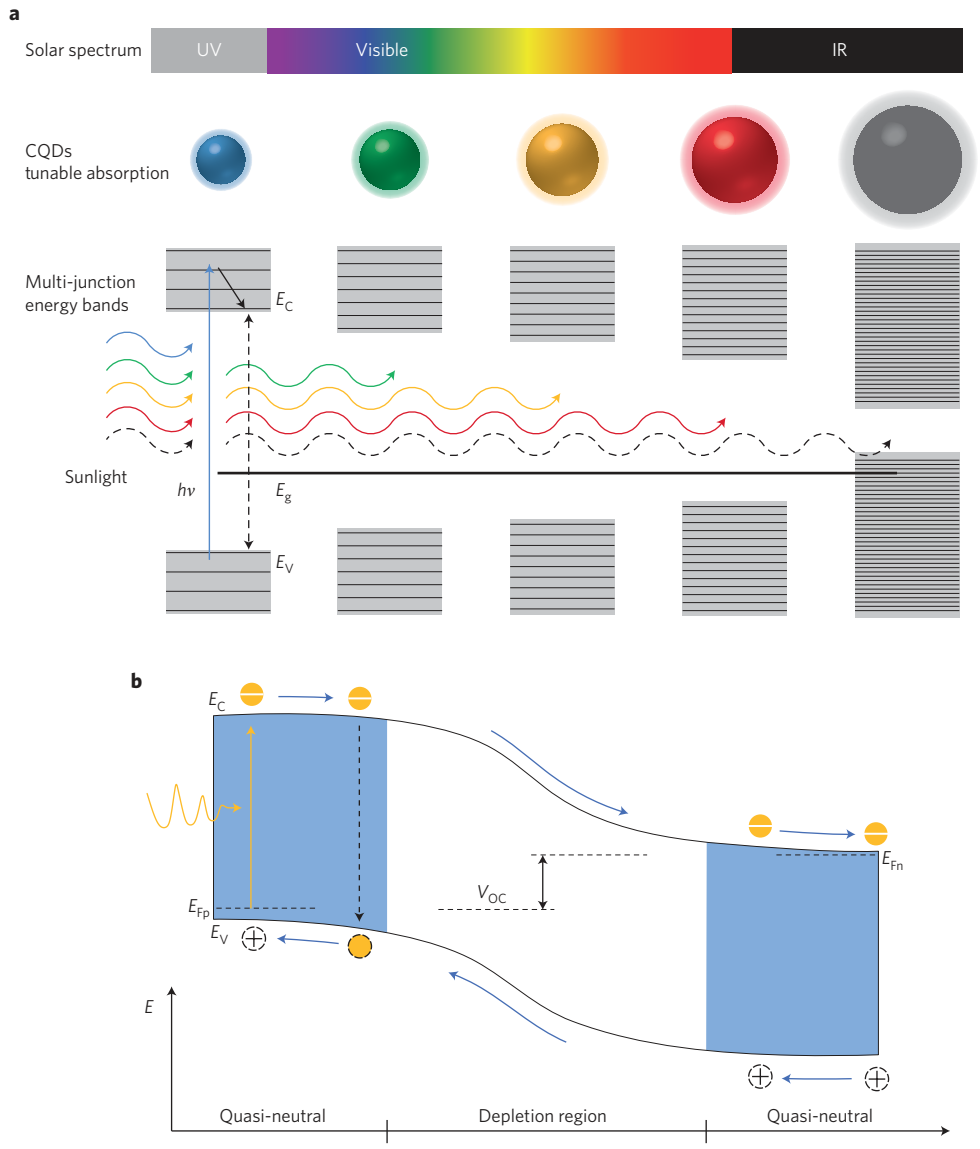

Figure 1 | Colloidal quantum dot photovoltaics. a, Size-dependent absorption enables CQDs to be tuned to absorb, sequentially, the constituent bands making up the Sun's broad spectrum, paving the way for the construction of multi-junction solar cells that overcome the energy loss in single-junction cells resulting from thermalization. This is achieved by reducing the discrepancy between the energy of absorbed photons ($h\nu$) and the bandgap (E_g, dashed black arrow) of the material in which they are absorbed, so that the energy lost by the photoexcitations due to thermalization (solid black arrow) is minimized. E_C and E_V are the conduction and valence band edges, respectively. **b**, Working principles of CQD solar cells. CQD device architectures take advantage of a p–n junction to produce a photovoltaic effect under optical illumination. A key challenge is in increasing the short diffusion length for minority carriers, which limits the practical thickness of the active layer in CQDs built on a planar electrode. The blue regions depict quasi-neutral regions, whereas band-bending occurs primarily in the depletion region (white). Photoelectrons generated in the p-type material on the left diffuse into the depletion region, through which they are swept by the action of an electric field and diffuse into the electron-collecting contact on the right. Photohole transport proceeds from right to left analogously. Orange arrows represent the photon absorption process. The dashed black arrow represents recombination, which must be slowed by improved quantum dot passivation, and overcome by efficient minority-carrier transport. E_{Fn} and E_{Fp} are the electron and hole quasi-Fermi levels, respectively.

efficiently collected. The diffusion length in CQD solids is reported to be in the range of 10–100 nm (ref. 35). For this reason, to retain efficient charge extraction, the thickness of the active CQD film cannot exceed the sum of minority-carrier diffusion length and depletion region. This limits the practical thickness of the CQD light-absorbing layer to about ~300 nm today. However, in light of the absorption coefficient available in the best CQD solids, complete absorption mandates an absorber thickness of ~1 μm (refs 8,36).

Structured electrodes for CQD photovoltaics

Bulk heterojunction structures used with great success in organic photovoltaics[37] suggest a path forward for improving CQD solar cell performance. Device architectures recently explored are shown in Fig. 2a,b, in which ordered and random porous structured electrodes are infiltrated with CQDs. The interpenetrating donor–acceptor structure allows for efficient charge separation even when optically thick CQD films are employed.

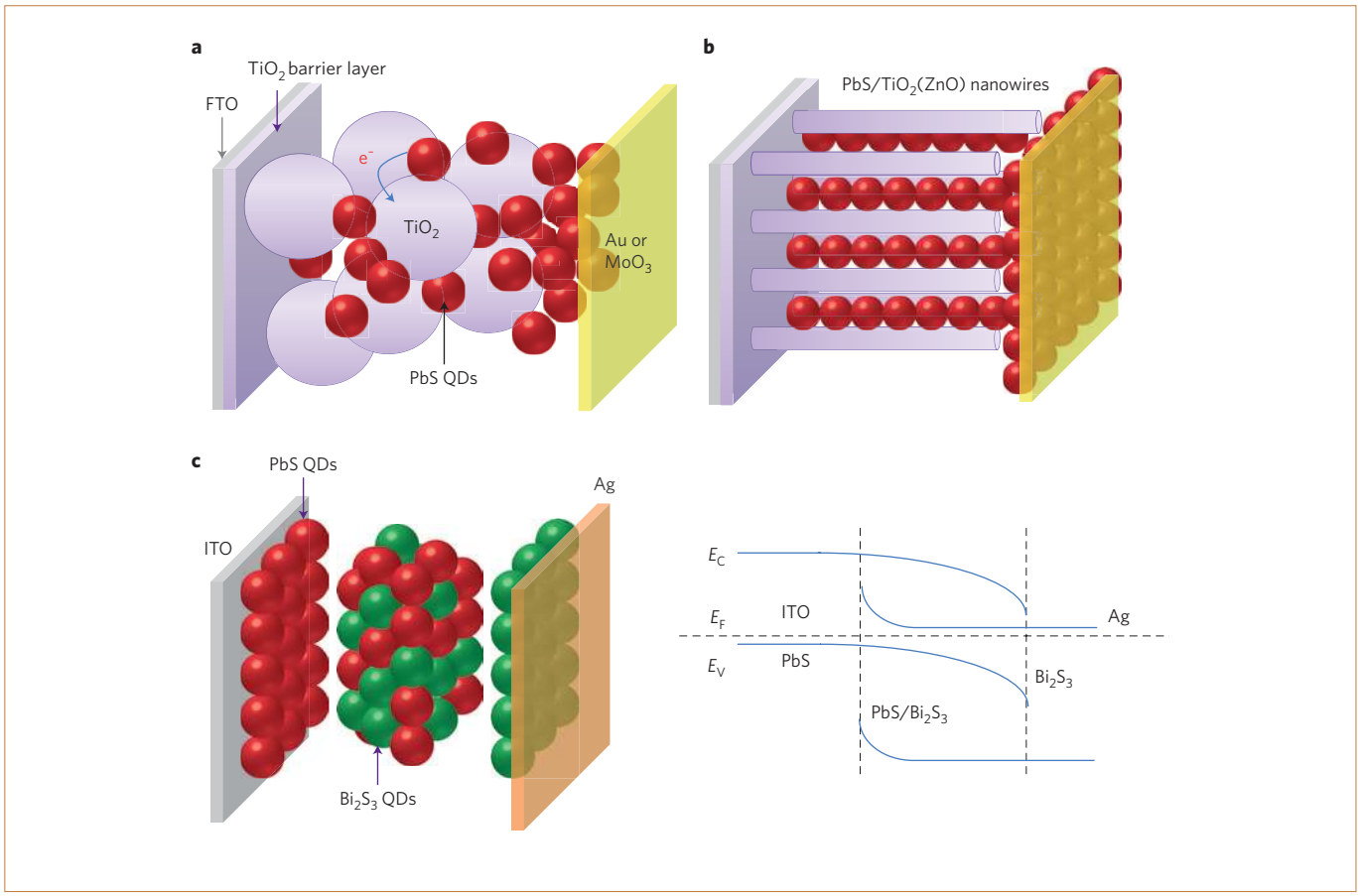

Figure 2 | Architectures for depleted bulk heterojunction quantum dot photovoltaics. a,**b**, Two types of structured electrode are generally used for infiltration of CQDs: porous structured electrode (**a**) and ordered one-dimensional nanostructure electrode (**b**). **c**, A blend of n-type Bi_2S_3 and p-type PbS CQDs was employed to form the interpenetrating bulk heterojunction structure (left). Holes flow to the left into the PbS, and electrons to the right into the Bi_2S_3, as reflected in the spatial band diagram (right).

An early prototype used ordered ZnO nanowires in conjunction with PbSe CQDs[38]. The results indicated that, for an equal areal cross-section of quantum dots, interpenetrating the ZnO nanowires with CQDs produced improved charge separation and collection from the CQD solid. This led to approximately three times higher photocurrent than in the planar case.

More performance-optimized depleted bulk heterojunction (DBH) devices employing a porous TiO_2 electrode were subsequently developed[39] (Fig. 2a). The porous electrode began with a layer of dense TiO_2 composed of small (10–30 nm) nanocrystals, followed by a paste of larger TiO_2 (150–250 nm) particles. The large-particle film acted as a porous scaffold into which CQDs infiltrated, thus forming an interpenetrating network of TiO_2 and CQDs. These DBH devices showed increased absorption, especially in the absorption-limited infrared wavelengths; however, the resultant DBH devices, showed poorer overall performance compared with planar cases. Accelerated recombination was identified as a cause, resultant from the larger interfacial area in the structure, suggesting the need to manage better this extended interface.

To explore further avenues of obtaining quantitatively improved performance from the DBH concept, ordered TiO_2 nanopillar electrodes were fabricated with the aid of electron-beam lithographically defined templates. These allowed for full infiltration of CQDs and a higher degree of control over the length scale on which phase separation was achieved[40]. The results confirmed that — in contrast with organic solar cells in which phase separation on the order of tens of nanometres is required — the length scale for interpenetrating material definition is very different in the CQD system: for efficient operation, the distance between adjacent nanopillars must fulfil the requirement $d_{np-np} \approx 2(W_{CQD} + L)$, where d_{np-np} is the space between adjacent nanopillars, W_{CQD} the depletion region width in the CQD film and L the diffusion length of minority carriers (electrons in the case of p-type CQD films).

These early studies catalysed a systematic effort to leverage the benefits of nanowires in CQD photovoltaics. A bottom-up defined, solution-processed TiO_2 nanowire network structured electrode was developed, which has the advantage of being easy to fabricate[41] (Fig. 2b). The structured electrode begins with the growth of ZnO nanowires that serve as a scaffold. Following deposition of a liquid phase, which involved mild etching of ZnO and simultaneous deposition of TiO_2, the nanowires were converted into porous TiO_2. A $TiCl_4$ treatment converted the porous tubular structure into a solid structure. The morphology of the resultant TiO_2 nanowire network electrode was thus determined by that of the starting ZnO nanowires, whereas the electronic properties were defined by the TiO_2 surface. Systematic morphological optimization led to nanowire lengths of ~300 nm and interbundle separations of similar order. These devices showed solar-power conversion efficiencies of 7.3±0.2%, a record at that time, and were superior to the planar reference case. The optimized DBH structure allowed the use of a notably thicker quantum dot film, enabled by the extended depletion region in the active layer resulting from the use of the infiltrated structured nanowire electrode.

In a parallel effort, ZnO-only nanowires were successfully integrated with CQDs in a device architecture consisting of indium tin oxide (ITO), a ZnO seed layer, ZnO nanowires, and a PbS CQD

active layer followed by a MoO_3/Au top contact[42]. By optimizing nanowire growth, including crystal quality, vertical alignment and large-area uniformity, a nanowire-based device was produced that achieved a 50% increase in short-circuit current density, and correspondingly a 35% enhancement in power conversion efficiency, over its planar counterpart, yielding a power conversion efficiency of 4.9%. In a recent work, comparatively long ZnO nanowires, on the order of one micrometre, were employed with particular emphasis on the manipulation of their structural parameters via modification of the ZnO seed layer[43]. The results suggest that an optimized DBH structure requires denser and thinner ZnO nanowires capable of successfully combining light absorption with charge extraction. A maximum incident-photon-to-current-conversion efficiency of 58% was obtained in the near infrared, with over 80% obtained in the visible region, leading to a power conversion efficiency of 6.0%.

Each of these studies pointed to the importance of further work to minimize recombination as the junction surface area was increased, and to the need for further work to achieve tall (micrometre) nanowires that are fully infiltrated with quantum dot light-absorbers.

On a related but distinct path, an all-solution-processed inorganic bulk nano-heterojunction structure was recently reported[44] (Fig. 2c). Attractively, this strategy used a liquid mixture of Bi_2S_3 and PbS CQDs to form the blended layer. At the interface between Bi_2S_3 nanocrystals and PbS quantum dots, holes are drawn into the PbS phase, and electrons into the Bi_2S_3 phase. Strikingly, a more than threefold improvement in performance was demonstrated compared with its bilayer counterpart. The performance enhancement arose from the extended carrier lifetime resulting from nanoscale phase separation. In this structure, both donor and acceptor materials acted as active, light-absorbing media. Hybrid photovoltaics that blend semiconducting polymers with CQDs have also seen continued attention[5,45–47]. This strategy has so far shown limited efficiencies, likely to be a consequence of impeded transport in the hybrid solid. Further advances in controlling phase segregation on the desired length scales offers the potential for simultaneous enhancements in the hybrid approach by leveraging charge separation via a well-engineered type-II bulk heterojunction, combined with the needed excellent electron and hole transport in the respective phases.

All of these bulk heterojunction strategies share a common set of requirements for further progress. In any phase in which light absorption, and thus photocarrier generation, occurs, the excitations must reach — be it by drift, diffusion or both — the charge-separating interface without recombining. This necessitates a transport length that exceeds the local thickness of the absorbing region(s) within the bulk heterojunction. The inter-materials interface must provide separation and must block backward recombination. Finally, each phase must offer sufficient mobility for its respective majority carrier to minimize series resistance and thus preserve high fill factor.

Engineering the CQD-to-bulk-material heterointerface

The preceding studies highlighted the need for improved control over electronic properties — most noteworthy, recombination — at the interface between the electrode and the CQD absorber. There have been multiple recent insights on this important topic that have enabled strides in performance.

One key area of progress has been the deepened understanding of how band offsets at the heterointerface, and carrier density in the bulk electrode, can be controlled by means of doping to produce more efficient charge separation[48,49]. Recent progress was made within the sol–gel materials processing system, an approach that enabled incorporation of a variety of different dopants into the TiO_2 host materials[48]. Employing Zr and Sb as dopants allowed control over the conduction band edge, progressively shifting it across the range –3.9 to –4.2 eV, compared with –3.8 eV for intrinsic TiO_2 (Fig. 3a). The Zr-doped TiO_2 with deeper electron affinity improved charge injection, leading to increased photocurrent and boosting performance. Further deepening of the conduction band provided no further benefit to carrier injection, and compromised the operating voltage *V*oc.

The free-carrier density in the bulk electron-acceptor material plays a critical role in forming the depletion region, and in particular in defining its thickness. This phenomenon was recently explored in a work looking at the transition from excitonic to p–n depleted-heterojunction operation, a progression mediated by ultraviolet (UV) exposure of the electrode in the ZnO/PbS system[49]. ZnO is generally intrinsic due to the trapping of mobile electrons by gas molecules, but can be turned n-type via UV exposure. Only when ZnO was photodoped to a free-carrier density near or greater than that of a PbS CQD film did a significant portion of the depletion region reside within the CQD layer. This study thus provided further confirmation of the depleted heterojunction picture of optimized CQD photovoltaic device operation.

Energy band engineering of transparent electrodes also found an important field of application in the multi-junction, quantum-tuned, CQD cells. The tunability of the CQD absorber is one of the principal advantages of this materials class: CQD absorber layers that have a number of size-programmed bandgaps can readily be stacked in a multi-junction cell architecture. A suitable selection of transparent electrode materials is needed to produce highly efficient recombination layers at the point of connection among the junctions having different bandgaps. This was recently achieved in a manner compatible with CQD materials processing via the advent of the graded recombination layer (GRL)[50]. The GRL consists of a progression of n-type transparent semiconductors with graded work functions, such as the series TiO_2–AZO–ITO–MoO_3, to connect front and back cells, thereby minimizing the barrier for photoholes from the ohmic side of one junction to recombine with photoelectrons from the electron-accepting side of the vertically adjacent junction (Fig. 3b). Following its first demonstration, GRL design has been refined through modelling that takes account of tunnelling and thermionic emission mechanisms as contributors to the current density across the layers[51,52]. These results suggest that a simplified material stack may be sufficient to enable low-resistance, hence high-fill-factor, multi-junction cell operation.

Recently, a donor-supply electrode (DSE) concept was proposed that leverages a two-layer material stack and charge-transfer doping, potentially enabling an all-room-temperature process urgently needed in multi-junction CQD devices[52]. Based on this concept, a new record performance of 8.5% was recently reported[53]. This new version of the depleted heterojunction device employed a shallow-work-function fluorine-doped tin oxide electrode beneath an ultrathin, low-doped TiO_2 electron acceptor. Experiments and simulations indicated that the work function of the final electrode, and the thickness of the intervening electron acceptor, can be controlled to extend the depleted region deeper into the quantum dot solid, leading to the improved performance.

Materials engineering of electrodes has seen a further recent advance, one in which transition metal oxides such as molybdenum trioxide (MoO_3) and vanadium pentoxide (V_2O_5) have been deployed as improved hole-extracting ohmic contacts to CQD films[54,55]. Interestingly, although the deep work function of these materials is well suited to their hole-extracting purpose, work function considerations alone are insufficient to explain the significantly improved low-resistance materials interface produced using transition metal oxides. The existence of an interface dipole can enhance band bending at the MoO_3/CQD interface, favouring extraction of holes from the MoO_3 side, as observed in organic optoelectronics[56]. Ultraviolet photoelectron spectroscopy studies suggest that gap states attributable to oxygen vacancies are present in the bandgap

of MoO_3, and that these may align well with the valence band of CQD films, offering an extra channel for hole removal[54]. Finally, high-work-function MoO_3 may pin the Fermi level of the top electrode, further enabling the desired ohmic contact[55]. The field of organic electronics has deepened the understanding of how MoO_3 achieves its benefits, with a recent study showing charge-transfer p-type doping of organic semiconductors by MoO_3, a consequence of the large electron affinity of MoO_3 of 6.7 eV (refs 57,58).

Shape control over the materials making up CQD solar cells represents a promising further frontier for progress. Metallic and semiconducting nanocrystals with controlled shapes have attracted great interest due to the intrinsic anisotropic property of crystalline materials. Control over the exposed facets on nanoparticle metal oxide electrode materials offers to bring improved performance in CQD solar cells, such as through the utilization of (001)–rich anatase TiO_2, whose high surface energy has long been associated with excellent photocatalytic properties[59]. Recently, the successful application of a (001)-rich anatase TiO_2 nanosheet as the acceptor material in a CQD cell was reported[60]. A notable step up in power conversion efficiency to 4.7% was achieved compared with 4.0% for the (101)-rich nanoparticle reference electrode. The improvement came from higher ionic charge of the exposed (001) facet compared with thermodynamically more stable (101) facets, thereby strengthening the attachment of CQDs to the TiO_2 surface.

Control over the electrode interface also suggests a pathway to a lowered recombination-centre density, a major limiter of CQD solar cell performance[61]. This was seen in quantum dot sensitized solar cells, in which electron–hole recombination at the TiO_2/hole-conductor interface was addressed using self-assembled monolayers of organic linkers[62] and inorganic coatings[63,64]. Here, the application of an engineered inorganic interfacial layer via atomic layer deposition (ALD) was simple, reproducible and resulted in a high degree of conformality in covering high-aspect-ratio structures[65]. A wide range of metal oxides, including Al_2O_3 and Ga_2O_3, have been employed to improve passivation of photoanode materials[66,67]. It is believed that the versatility of materials that can be used in ALD can also be leveraged to enhance carrier mobility within the CQD solid by lowering the height of the energetic barrier for inter-quantum-dot transport (Fig. 3c). ALD coating for encapsulation has also produced a convenient, integrated packaging technology to increase the lifetime of CQD cells. Atomic layer deposition of Al_2O_3 provided an excellent barrier to gas permeation, inhibiting oxidation and photothermal degradation of CQD films[68–70]. Encapsulation technologies, extensively investigated and now widely deployed in organic solar cells, are of high importance in CQD solar technology with similarly demanding requirements on cost, longevity and performance.

Insertion of an interface layer between CQDs and a Schottky electrode was recently found to enhance *V*oc (ref. 71), leading to values approaching 0.7 V. Similarly, high *V*oc approaching 60–75% of its theoretical maximum value has been achieved in comparatively clean-bandgap CISe quantum dot solar cells[72]. These works suggest promising avenues to further increasing *V*oc, which has much room for further improvement.

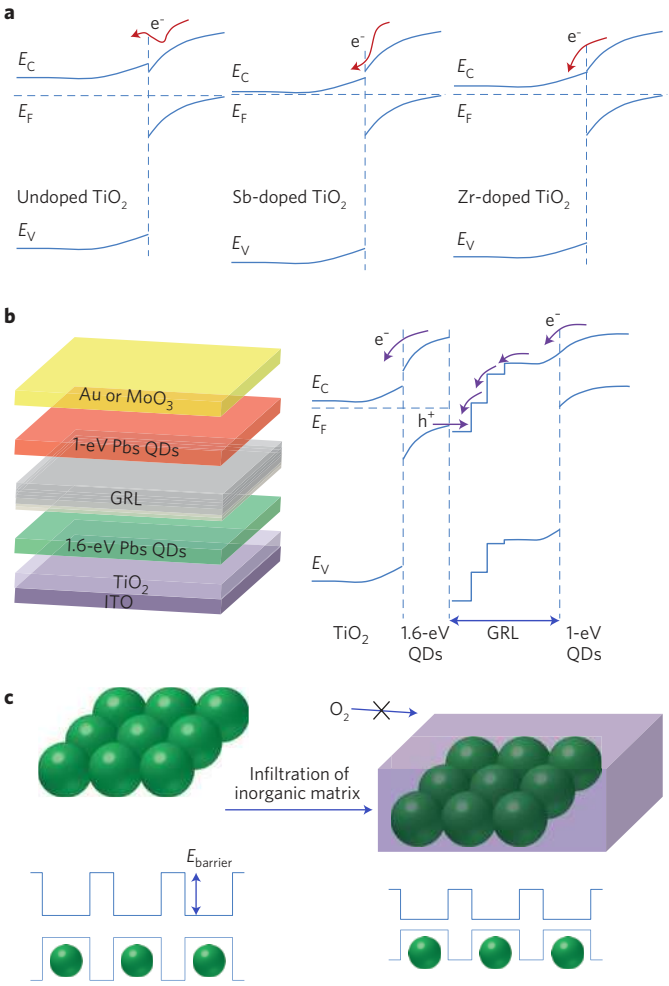

Figure 3 | Engineering the electronics of the CQD/electrode interface. **a**, The desired band alignment at the heterointerface to achieve efficient charge separation without excessive thermalization of electrons as they cross the junction. **b**, The graded recombination layer (GRL) was developed to enable tandem and, ultimately, multi-junction solar cells. The GRL allows hole current from the 1.6-eV PbS QD front cell and the electron current from the 1.0-eV PbS QD back cell to recombine with high efficiency and minimal loss of electrical potential. **c**, Infiltration of inorganic matrix via atomic layer deposition addressed the challenge of high internal surface area, and protected CQDs against oxidative and photothermal damage, promoting the stability of the resulting devices. The bottom panels illustrate how an inorganic matrix (purple) can infiltrate a quantum dot solid (green) to militate against the ingress of oxygen. This may also reduce the energetic barrier ($E_{barrier}$) seen by electrons or by holes. Panel **a** reproduced with permission from ref. 48, © 2011 Wiley.

Quantum-tuned rectifying junctions

It was recently recognized that reliance on a bulk material as an electrode in forming a rectifying junction with a CQD solid comes with a significant limitation. When the quantum dot layer is size-tuned to a new bandgap, the bulk electrode must be re-optimized.

An all-quantum-tuned cell, wherein the charge-separating junction was made using two inherently band-aligned materials, would be highly desirable as a result. This, however, would rely on the availability of photovoltaics-quality CQD materials that could be alternately doped p- or n-type.

Fortunately, the needed advances on doping control in CQD solids have recently been made. A model of CQD doping, called the charge–orbital balance model[73], predicts doping type and level based on the overall stoichiometry of a CQD solid, taking into account the contributions of both inorganic species and organic ligands. It begins with determination of the number of valence electrons available in the CQD film system and comparing it with the number of orbitals in the valence shell for filling of valence electrons. Complete filling of the valence orbitals results in a closed electronic shell configuration and leads to an intrinsic material. An excess of electrons residing in the conduction band results in n-type doping, whereas incomplete filling of the valence band leads to p-type doping. Bulk metal–chalcogen binary compound semiconductors thus are n-type when they are off-stoichiometric because of a metal cation excess[74].

The PbS CQDs widely studied in CQD photovoltaics have been observed to exhibit a lead excess, a consequence of the synthetic

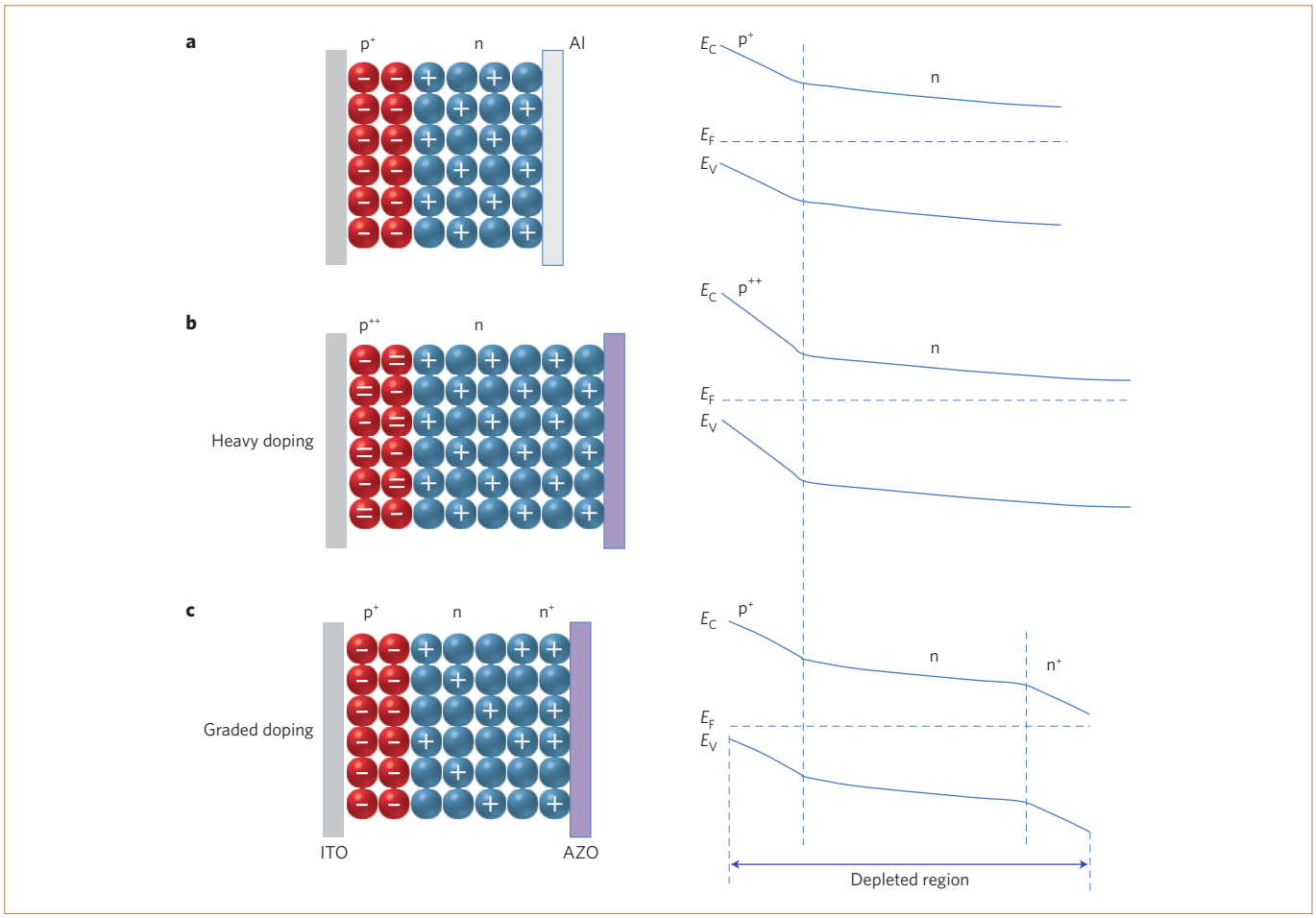

Figure 4 | The quantum junction solar cell. Such solar cells take advantage of quantum-tuned solids on each side of the junction, facilitating tunable matching to the broad visible and infrared solar spectrum. **a**, First prototypes employed higher-doped p-type PbS CQDs and lighter-doped n-type PbS CQDs to demonstrate the concept, and a certified power conversion efficiency of 5.4% was achieved. The p-type material is ohmically contacted using a material such as ITO; and the n-type material using shallow work function materials such as Al or AZO. **b**, Increasing the doping density of the p-side by chemical doping enabled extension of the n-side portion of the depletion region, allowing the use of a greater thickness of the light-absorbing material. **c**, A cascaded band alignment enabled by graded doping benefits Fermi level splitting and thus increases the photoinduced voltage, while the resultant enhanced built-in electric field favours charge collection at the maximum power point of solar cell operation. The schematics on the right depict spatial band diagrams at equilibrium for each device architecture (left). Vertical dashed lines denote the compositional junction between the differently doped regions of the semiconductor.

protocol in which the coordinating ligand binds only the cation and not the anion[75]. This fact has motivated researchers to find better means to passivate the surface of the nanoparticle, and thus to maintain its intrinsic n-type behaviour. It was recently found that n-type PbS CQD films can be achieved using atomic passivation[76], wherein inorganic halide anions (for example, Cl^-, Br^-, I^-) increased the overall passivation of surface dangling bonds when films were processed in an inert atmosphere. X-ray photoelectron spectroscopy confirmed that a considerable amount of halide was incorporated in the form of a Pb–halide bond, indicating substitutional doping. This produced n-type doping in accordance with the charge–orbital balance model. Chemical treatments have also been demonstrated to tune the p-type doping of PbSe nanocrystals[77]. Exposure of the nanocrystal film to a suitably designed redox couple was used to manipulate the doping density. Reversible charge transfer, and thus reversible doping, was accomplished by varying the potential of the redox buffer solution, leading to widely tunable carrier density. More recently, another work has reported heavily doped n-type PbSe and PbS nanocrytals[78] in which persistent n-type doping was achieved via ground-state electron transfer from the reducing agent cobaltocene.

With the benefit of new found control over doping in photovoltaic-quality films, it became possible to build solar cells in which each side of the rectifying junction leveraged size-effect tuning[79]. These quantum junction solar cells began with a p-type CQD layer atop ITO-coated glass, which was followed by a doped n-layer to form a p–n junction. An Al–Ag bilayer electrode completed the device (Fig. 4a). This architecture allowed for a built-in electric field that formed at the p–n junction and for a significant depletion region extending into each side of the light-absorbing medium. In this architecture, the inherent matching of bandgaps enables wide tuning while automatically preserving optimal band alignment between the p and n layers. Early prototypes rapidly produced certified AM1.5 solar-power conversion efficiencies of 5.4%.

The quantum junction concept has seen a number of refinements since these early studies. The first relates to the choice of the electrical contact with the n-type layer. Initially Al was employed to form the ohmic contact to the CQD n-type film; however, Al tends to react with those halides that are essential to the passivation and doping of the CQD film. Use of a shallow-work-function-doped metal oxide electrode in place of Al overcame these interface issues and offered a hole-blocking layer at the cathode interface[80]. The

second advance related to deepening the depletion region depth to increase charge-collection efficiency: heavily doped p-type CQDs were created by substituting Ag for Pb during the synthesis procedure[80], leading to orders-of-magnitude increase in doping density over previous levels (Fig. 4b) and thereby improving charge collection in the visible and especially the infrared region of the solar spectrum. Finally, further refinements in control over doping density have enabled rational design of multilayered device architectures: a cascade-graded CQD structure recently introduced a heavily doped n^+ layer on the back side of the cell[27] (Fig. 4c), where control over the n-type doping level across the range 10^{16}–10^{17} cm^{-3} was achieved by finely tuning the halide treatment. The thin and heavily doped n^+ layer resulted in an increased electric field at the rear of the device, facilitating photocarrier extraction in the position at which improvement was most required. The more heavily doped layer also enhanced quasi-Fermi-level splitting at the maximum power point, resulting in increased operating voltage.

Future prospects

Progress in materials chemistry of the CQD active layer has been a central front in advancing CQD device performance. The present work instead examined how insights into device architecture, combined with materials chemical manipulation of the stack that makes up nanostructured CQD solar cells, can in parallel enhance solar cell performance.

Much room remains to advance further the concepts reviewed herein, and to bring new ideas to the field. The full potential of structured-electrode-based devices will require progress on a number of fronts. Ideally, the electron-extracting electrode will provide high majority-carrier mobilities for low series resistance, combined with high doping levels with the goal of achieving deep depletion of the absorber throughout its entire volume. The absorber itself will benefit from being made conformal with the structured electrode, thereby enabling penetration of the hole-collecting electrode into the opposite side of the active layer, thus overcoming any limitations to hole transport as well. The hole-collecting electrode will in turn offer the needed high hole mobility, electron blocking and reduced optical absorption.

The advent of photovoltaic-quality p- and n-type CQD materials of varied doping levels, combined with increased understanding of their band relationships with various metal oxides, creates an important materials integration opportunity for the field. As CQD solar cells approach a 10% single-junction solar-power conversion efficiency, a renewed attempt at building highly optimized tandem and multi-junction cells that can then extend performance to 15% and beyond through improved spectral utilization will see increased focus.

Received 3 January 2013; accepted 22 October 2013; published online 20 February 2014

References

1. Wenham, S. R. & Green, M. A. Silicon solar cells. *Prog. Photovoltaics Res. Appl.* **4,** 3–33 (1996).
2. Romeo, N., Bosio, A., Canevari, V. & Podesta, A. Recent progress on CdTe/CdS thin film solar cells. *Sol. Energy* **77,** 795–801 (2004).
3. O'Regan, B. & Grätzel, M. A low-cost, high-efficiency solar cell based on dye-sensitized colloidal TiO_2 films. *Nature* **353,** 737–740 (1991).
4. Nelson, J. Polymer: fullerene bulk heterojunction solar cells. *Mater. Today* **14,** 462–470 (October, 2011).
5. Günes, S. & Sariciftci, N. S. Hybrid solar cells. *Inorg. Chim. Acta* **361,** 581–588 (2008).
6. Santra, P. K. & Kamat, P. V. Mn-doped quantum dot sensitized solar cells: a strategy to boost efficiency over 5%. *J. Am. Chem. Soc.* **134,** 2508–2511 (2012).
7. McDonald, S. A. *et al.* Solution-processed PbS quantum dot infrared photodetectors and photovoltaics. *Nature Mater.* **4,** 138–142 (2005).
8. Tang, J. & Sargent, E. H. Infrared colloidal quantum dots for photovoltaics: fundamentals and recent progress. *Adv. Mater.* **23,** 12–29 (2011).
9. Alivisatos, A. P. Semiconductor clusters, nanocrystals, and quantum dots. *Science* **271,** 933–937 (1996).
10. Semonin, O. E. *et al.* Peak external photocurrent quantum efficiency exceeding 100% via MEG in a quantum dot solar cell. *Science* **334,** 1530–1533 (2011).
11. Huang, X., Han, S., Huang, W. & Liu, X. Enhancing solar cell efficiency: the search for luminescent materials as spectral converters. *Chem. Soc. Rev.* **42,** 173–201 (2013).
12. Shockley, W. & Queisser, H. J. Detailed balance limit of efficiency of p–n junction solar cells. *J. Appl. Phys.* **32,** 510–519 (1961).
13. Barkhouse, D. A. R., Pattantyus-Abraham, A. G., Levina, L. & Sargent, E. H. Thiols passivate recombination centers in colloidal quantum dots leading to enhanced photovoltaic device efficiency. *ACS Nano* **2,** 2356–2362 (2008).
14. Kovalenko, M. V., Scheele, M. & Talapin, D. V. Colloidal nanocrystals with molecular metal chalcogenide surface ligands. *Science* **324,** 1417–1420 (2009).
15. Law, M. *et al.* Structural, optical, and electrical properties of PbSe nanocrystal solids treated thermally or with simple amines. *J. Am. Chem. Soc.* **130,** 5974–5985 (2008).
16. Lee, J. S., Kovalenko, M. V., Huang, J., Chung, D. S. & Talapin, D. V. Band-like transport, high electron mobility and high photoconductivity in all-inorganic nanocrystal arrays. *Nature Nanotech.* **6,** 348–352 (2011).
17. Owen, J. S., Park, J., Trudeau, P.-E. & Alivisatos, A. P. Reaction chemistry and ligand exchange at cadmium–selenide nanocrystal surfaces. *J. Am. Chem. Soc.* **130,** 12279–12281 (2008).
18. Talapin, D. V. & Murray, C. B. PbSe nanocrystal solids for n- and p-channel thin film field-effect transistors. *Science* **310,** 86–89 (2005).
19. Liu, Y. *et al.* Dependence of carrier mobility on nanocrystal size and ligand length in PbSe nanocrystal solids. *Nano Lett.* **10,** 1960–1969 (2010).
20. Luther, J. M. *et al.* Structural, optical, and electrical properties of self-assembled films of PbSe nanocrystals treated with 1,2-ethanedithiol. *ACS Nano* **2,** 271–280 (2008).
21. Nagpal, P. & Klimov, V. I. Role of mid-gap states in charge transport and photoconductivity in semiconductor nanocrystal films. *Nature Commun.* **2,** 486 (2011).
22. Tang, J. *et al.* Colloidal-quantum-dot photovoltaics using atomic-ligand passivation. *Nature Mater.* **10,** 765–771 (2011).
23. Bae, W. K. *et al.* Highly effective surface passivation of PbSe quantum dots through reaction with molecular chlorine. *J. Am. Chem. Soc.* **134,** 20160–20168 (2012).
24. Ning, Z. *et al.* All-inorganic colloidal quantum dot photovoltaics employing solution-phase halide passivation. *Adv. Mater.* **24,** 6295–6299 (2012).
25. Ip, A. H. *et al.* Hybrid passivated colloidal quantum dot solids. *Nature Nanotech.* **7,** 577–582 (2012).
26. Steim, R., Kogler, F. R. & Brabec, C. J. Interface materials for organic solar cells. *J. Mater. Chem.* **20,** 2499–2512 (2010).
27. Ning, Z. *et al.* Graded doping for enhanced colloidal quantum dot photovoltaics. *Adv. Mater.* **25,** 1719–1723 (2013).
28. Yip, H.-L. & Jen, A. K. Y. Recent advances in solution-processed interfacial materials for efficient and stable polymer solar cells. *Energy Environ. Sci.* **5,** 5994–6011 (2012).
29. Luther, J. M. *et al.* Schottky solar cells based on colloidal nanocrystal films. *Nano Lett.* **8,** 3488–3492 (2008).
30. Johnston, K. W. *et al.* Efficient Schottky-quantum-dot photovoltaics: The roles of depletion, drift, and diffusion. *Appl. Phys. Lett.* **92,** 122111–122113 (2008).
31. Ma, W. *et al.* Photovoltaic performance of ultrasmall PbSe quantum dots. *ACS Nano* **5,** 8140–8147 (2011).
32. Pattantyus-Abraham, A. G. *et al.* Depleted-heterojunction colloidal quantum dot solar cells. *ACS Nano* **4,** 3374–3380 (2010).
33. Luther, J. M. *et al.* Stability assessment on a 3% bilayer PbS/ZnO quantum dot heterojunction solar cell. *Adv. Mater.* **22,** 3704–3707 (2010).
34. Chang, L.-Y., Lunt, R. R., Brown, P. R., Bulović, V. & Bawendi, M. G. Low-temperature solution-processed solar cells based on PbS colloidal quantum dot/CdS heterojunctions. *Nano Lett.* **13,** 994–999 (2013).
35. Koleilat, G. I. *et al.* Efficient, stable infrared photovoltaics based on solution-cast colloidal quantum dots. *ACS Nano* **2,** 833–840 (2008).
36. Sargent, E. H. Colloidal quantum dot solar cells. *Nature Photon.* **6,** 133–135 (2012).
37. Park, S. H. *et al.* Bulk heterojunction solar cells with internal quantum efficiency approaching 100%. *Nature Photon.* **3,** 297–302 (2009).
38. Leschkies, K. S., Jacobs, A. G., Norris, D. J. & Aydil, E. S. Nanowire-quantum-dot solar cells and the influence of nanowire length on the charge collection efficiency. *Appl. Phys. Lett.* **95,** 193103 (2009).
39. Barkhouse, D. A. R. *et al.* Depleted bulk heterojunction colloidal quantum dot photovoltaics. *Adv. Mater.* **23,** 3134–3138 (2011).
40. Kramer, I. J. *et al.* Ordered nanopillar structured electrodes for depleted bulk heterojunction colloidal quantum dot solar cells. *Adv. Mater.* **24,** 2315–2319 (2012).

41. Lan, X. *et al.* Self-assembled, nanowire network electrodes for depleted bulk heterojunction solar cells. *Adv. Mater.* **25,** 1769–1773 (2013).
42. Jean, J. *et al.* ZnO nanowire arrays for enhanced photocurrent in PbS quantum dot solar cells. *Adv. Mater.* **25,** 2790–2796 (2013).
43. Wang, H., Kubo, T., Nakazaki, J., Kinoshita, T. & Segawa, H. PbS-quantum-dot-based heterojunction solar cells utilizing ZnO nanowires for high external quantum efficiency in the near-infrared region. *J. Phys. Chem. Lett.* **4,** 2455–2460 (2013).
44. Rath, A. K. *et al.* Solution-processed inorganic bulk nano-heterojunctions and their application to solar cells. *Nature Photon.* **6,** 529–534 (2012).
45. Wei, H., Zhang, H., Sun, H. & Yang, B. Preparation of polymer–nanocrystals hybrid solar cells through aqueous approaches. *Nano Today* **7,** 316–326 (2012).
46. Wright, M. & Uddin, A. Organic–inorganic hybrid solar cells: A comparative review. *Sol. Energ. Mater. Sol. C* **107,** 87–111 (2012).
47. Gao, F., Ren, S. & Wang, J. The renaissance of hybrid solar cells: progresses, challenges, and perspectives. *Energy Environ. Sci.* **6,** 2020–2040 (2013).
48. Liu, H. *et al.* Electron acceptor materials engineering in colloidal quantum dot solar cells. *Adv. Mater.* **23,** 3832–3837 (2011).
49. Willis, S. M., Cheng, C., Assender, H. E. & Watt, A. A. R. The transitional heterojunction behavior of PbS/ZnO colloidal quantum dot solar cells. *Nano Lett.* **12,** 1522–1526 (2012).
50. Wang, X. *et al.* Tandem colloidal quantum dot solar cells employing a graded recombination layer. *Nature Photon.* **5,** 480–484 (2011).
51. Koleilat, G. I., Wang, X. & Sargent, E. H. Graded recombination layers for multijunction photovoltaics. *Nano Lett.* **12,** 3043–3049 (2012).
52. Koleilat, G. I. *et al.* A donor-supply electrode (DSE) for colloidal quantum dot photovoltaics. *Nano Lett.* **11,** 5173–5178 (2011).
53. Maraghechi, P. *et al.* The donor-supply electrode enhances performance in colloidal quantum dot solar cells. *ACS Nano* **7,** 6111–6116 (2013).
54. Gao, J. *et al.* n-type transition metal oxide as a hole extraction layer in PbS quantum dot solar cells. *Nano Lett.* **11,** 3263–3266 (2011).
55. Brown, P. R. *et al.* Improved current extraction from ZnO/PbS quantum dot heterojunction photovoltaics using a MoO_3 interfacial layer. *Nano Lett.* **11,** 2955–2961 (2011).
56. Irfan *et al.* Energy level evolution of molybdenum trioxide interlayer between indium tin oxide and organic semiconductor. *Appl. Phys. Lett.* **96,** 073304–073303 (2010).
57. Lee, T. H. *et al.* p-channel field-effect transistors based on C_{60} doped with molybdenum trioxide. *ACS Appl. Mater. Interfaces* **5,** 2337–2341 (2013).
58. Gwinner, M. C. *et al.* Doping of organic semiconductors using molybdenum trioxide: a quantitative time-dependent electrical and spectroscopic study. *Adv. Funct. Mater.* **21,** 1432–1441 (2011).
59. Yang, H. G. *et al.* Solvothermal synthesis and photoreactivity of anatase TiO_2 nanosheets with dominant {001} facets. *J. Am. Chem. Soc.* **131,** 4078–4083 (2009).
60. Etgar, L. *et al.* High efficiency quantum dot heterojunction solar cell using anatase (001) TiO_2 nanosheets. *Adv. Mater.* **24,** 2202–2206 (2012).
61. Graetzel, M., Janssen, R. A. J., Mitzi, D. B. & Sargent, E. H. Materials interface engineering for solution-processed photovoltaics. *Nature* **488,** 304–312 (2012).
62. Ardalan, P. *et al.* Effects of self-assembled monolayers on solid-state CdS quantum dot sensitized solar cells. *ACS Nano* **5,** 1495–1504 (2011).
63. Son, H.-J. *et al.* Glass-encapsulated light harvesters: More efficient dye-sensitized solar cells by deposition of self-aligned, conformal, and self-limited silica layers. *J. Am. Chem. Soc.* **134,** 9537–9540 (2012).
64. McDaniel, H., Fuke, N., Pietryga, J. M. & Klimov, V. I. Engineered $CuInSe_xS_{2-x}$ quantum dots for sensitized solar cells. *J. Phys. Chem. Lett.* **4,** 355–361 (2013).
65. Marichy, C., Bechelany, M. & Pinna, N. Atomic layer deposition of nanostructured materials for energy and environmental applications. *Adv. Mater.* **24,** 1017–1032 (2012).
66. Hanson, K. *et al.* Stabilization of $[Ru(bpy)_2(4,4'\text{-}(PO_3H_2)bpy)]^{2+}$ on mesoporous TiO_2 with atomic layer deposition of Al_2O_3. *Chem. Mater.* **25,** 3–5 (2012).
67. Chandiran, A. K. *et al.* Subnanometer Ga_2O_3 tunnelling layer by atomic layer deposition to achieve 1.1 V open-circuit potential in dye-sensitized solar cells. *Nano Lett.* **12,** 3941–3947 (2012).
68. Ihly, R., Tolentino, J., Liu, Y., Gibbs, M. & Law, M. The photothermal stability of PbS quantum dot solids. *ACS Nano* **5,** 8175–8186 (2011).
69. Liu, Y. *et al.* Robust, functional nanocrystal solids by infilling with atomic layer deposition. *Nano Lett.* **11,** 5349–5355 (2011).
70. Liu, Y. *et al.* PbSe quantum dot field-effect transistors with air-stable electron mobilities above 7 $cm^2\ V^{-1}\ s^{-1}$. *Nano Lett.* **13,** 1578–1587 (2013).
71. Yoon, W. *et al.* Enhanced open-circuit voltage of PbS nanocrystal quantum dot solar cells. *Sci. Rep.* **3,** 2225 (2013).
72. Panthani, M. G. *et al.* $CuInSe_2$ quantum dot solar cells with high open-circuit voltage. *J. Phys. Chem. Lett.* **4,** 2030–2034 (2013).
73. Voznyy, O. *et al.* A charge-orbital balance picture of doping in colloidal quantum dot solids. *ACS Nano* **6,** 8448–8455 (2012).
74. Allgaier, R. S. & Scanlon, W. W. Mobility of electrons and holes in PbS, PbSe, and PbTe between room temperature and 4.2 K. *Phys. Rev.* **111,** 1029–1037 (1958).
75. Ma, W., Luther, J. M., Zheng, H., Wu, Y. & Alivisatos, A. P. Photovoltaic devices employing ternary PbS_xSe_{1-x} nanocrystals. *Nano Lett.* **9,** 1699–1703 (2009).
76. Zhitomirsky, D. *et al.* N-Type colloidal-quantum-dot solids for photovoltaics. *Adv. Mater.* **24,** 6181–6185 (2012).
77. Engel, J. H., Surendranath, Y. & Alivisatos, A. P. Controlled chemical doping of semiconductor nanocrystals using redox buffers. *J. Am. Chem. Soc.* **134,** 13200–13203 (2012).
78. Koh, W.-k. *et al.* Heavily doped n-type PbSe and PbS nanocrystals using ground-state charge transfer from cobaltocene. *Sci. Rep.* **3,** 2004 (2013).
79. Tang, J. *et al.* Quantum junction solar cells. *Nano Lett.* **12,** 4889–4894 (2012).
80. Liu, H. *et al.* Systematic optimization of quantum junction colloidal quantum dot solar cells. *Appl. Phys. Lett.* **101,** 151112–151113 (2012).

Acknowledgements

The authors acknowledge J. Xu for his contributions to the figures. This publication is based in part on work supported by Award KUS-11-009-21, made by King Abdullah University of Science and Technology (KAUST), the Ontario Research Fund Research Excellence Program, the Natural Sciences and Engineering Research Council (NSERC) of Canada, and Angstrom Engineering and Innovative Technology. X.L. would like to acknowledge a scholarship from the China Scholarship Council (CSC).

Additional information

Reprints and permissions information is available online at www.nature.com/reprints. Correspondence should be addressed to E.H.S.

Competing financial interests

The authors declare no competing financial interests.